Analysis and Design of a High Frequency Wireless Battery Charging System With Smooth Mode Transition Characteristics

Zhan Sun, *Student Member, IEEE*, Yingchao Chi, *Graduate Student Member, IEEE*, Yijie Wang, *Senior Member, IEEE*, Yueshi Guan, *Senior Member, IEEE*, and Dianguo Xu, *Fellow, IEEE*

***Abstract*—With the improvement of wireless power transfer technology has been widely used. The scheme of realizing wireless battery charging based on Class-E converter has gradually attracted attention. In this article, a detailed analysis is carried out for high-frequency system impedance compression technology, input voltage adaptability, compensation network structure, circuit stress, and sensitivity. The difficulties in realizing constant current/constant voltage adaptive charging with traditional design methods are summarized. To this end, a dual-channel system design method based on power synthesis technology is proposed, with a highly sensitive 6.78 MHz system assisted by a robust 500 kilohertz (kHz) subsystem. Combined with the traditional high-frequency passive constant-voltage impedance compression technology, the kHz subsystem provides active state locking, active load compression, and power adaptive compensation to achieve smooth impedance connection during mode switching, thereby completing safe and efficient battery charging. In order to verify the feasibility of the proposed method, a 170 W experimental prototype was built to simulate the charging process of the battery at 45–72 V/2.4 A and 72 V/2.4–0.3 A. The system maximum efficiency reaches 92%. The soft switching characteristics of the power amplifier and system efficiency are still guaranteed under a wide range of load variation, and an approximately ideal battery charging curve is output.**

***Index Terms*—Active state locking, constant current/constant voltage adaptive charging, impedance compression, power synthesis, smooth impedance connection, wireless power transfer.**

I. Introduction

In RECENT years, research on wireless power transfer (WPT) technology has become a hot spot. Resonant design approach was adopted to improve the system power conversion efficiency [1], [2], [3], [4]. WPT technology is widely used in various fields [5], [6], [7], [8], [9], such as underwater loads, electric vehicles, and biomedicine. Among them, battery charging is one of the main applications [10]. Considering battery life and safe operation, most traditional charging process of batteries is mainly divided into two stages, namely constant current mode (CCM) and constant voltage mode (CVM). Besides, a multilevel constant current (MSCC) charging mode was proposed to utilize multihigh harmonic for power transfer [11]. The inherent load-independent constant current output and zero phase angle (ZPA) input characteristics were maintained. By setting the combined mode of switching frequency and phase relationship of the bridge arm, the current can be converted to different levels for different stages of CC charging.

At present, most wireless power transfer systems can only achieve one of the CC or CV outputs without using additional means, especially high-frequency systems. Therefore, most research on battery charging mainly revolve around the realization of CC/CV output. To this end, methods have been proposed to tune the resonant circuit by increasing the number of passive components, switches, or relays [12], [13], [14], [15], [16]. A multicoil structure was employed and constituted a reconfigurable intermediate resonant circuit with additional switches for mode switching [12]. ZPA can be implemented in both CCM and CVM. However, the mutual inductance of the coil seriously affects the accuracy of the charging current and voltage, and has higher requirements on the coupling state. Meanwhile, due to the mode switching in the resonant cavity, the switch often needs higher withstand voltage stress and faces certain operational risks. Two intermediate coils were added to form a four-coil structure, which increases the effective magnetization impedance between the coils and improves the transmission efficiency [13]. The resonant tank was designed to achieve CCM and CVM charging at two different frequencies, respectively. However, frequency regulation is often accompanied by system stability issues.

In [14], a fixed operating frequency was adopted, and a relay was used to switch between three-coil and two-coil structures to realize CC and CV output. In [15], the *LCC*-S topology was reconfigured into an S–S topology by using three resonant circuits, and only relays were used to achieve CC/CV output, while the system also worked at a single frequency. In [16], a new compensation method with an inductor array was proposed to ensure that the input impedance of the system is inductive and reduces switching losses. Taking advantage of the

Manuscript received 14 February 2023; revised 11 June 2023; accepted 25 July 2023. Date of publication 1 August 2023; date of current version 22 September 2023. This work was supported in part by the National Natural Science Foundation of China under Grant 51922033, in part by the Power Electronics Science and Education Development Program of Delta Group under Grant DREK2020003, and in part by the Natural Science Foundation of Heilongjiang Province under Grant YQ2020E017. Recommended for publication by Associate Editor G. A. Covic. *(Corresponding author: Yijie Wang.)*

The authors are with the School of Electrical Engineering and Automation, Harbin Institute of Technology, Harbin 150001, China (e-mail: 21b906030@stu.hit.edu.cn; yingchaochi@163.com; wangyijie@hit.edu.cn; hitguanyueshi@163.com; xudiang@hit.edu.cn).

Color versions of one or more figures in this article are available at https://doi.org/10.1109/TPEL.2023.3300924.

Digital Object Identifier 10.1109/TPEL.2023.3300924

load-independent characteristics, the mathematical relationship between the passive components was derived, thereby reducing component count.

In addition to changing the circuit structure, the CCM/CVM of the battery can also be realized by adjusting the control strategy. In the case of introducing a resonant converter, a wide range of frequency variation is unavoidable. Variable frequency phase-shift control was proposed [17], and a new three-loop control strategy was adopted to make the system run at any point in the optimal operating frequency range. In [18], a full-bridge inverter controlled by a phase-synchronous method was used as a negative resistor to achieve power regulation without an additional dc–dc converter. The transmitting side controls the ON-OFF of the switch by measuring the operating frequency and the effective value of the input current, and does not require double-sided communication for real-time output current/voltage regulation. The robustness to load resistance and coupling coefficient variation has been improved.

Various load parameter identification methods are also an option, so as to obtain the equivalent load resistance, simplify the model, and realize CC/CV output. In [19], the input impedance characteristics of the nonpure resistance of the rectifier was considered. Output current, output voltage, and system equivalent resistance were identified. Combined with the output characteristics of the *LCC*-N structure, the relationship between the input and the output was simplified through the linear superposition of the fundamental wave and the third harmonic. The load output independent characteristic was realized through the linear control of the primary side. In [20], a load identification method realized by an orthogonal transformation algorithm and reflection impedance theory was proposed. The equivalent load resistance is obtained by using the active power and current of the primary side. The CCM/CVM is realized through the phase-shift control of the full-bridge inverter.

In this article, a novel battery charging design method is proposed to solve the difficulties encountered in traditional high-frequency WPT design methods (Nonuniform impedance compression direction, nonuniform network structure, nonuniform input voltage, and high voltage stress). Specifically, Section II gives the design methods of the traditional 6.78 M system to achieve CC and CV output, respectively, and analyzes the difficulties of simultaneous CC/CV implementation detailly. Section III gives the operating principles and advantages of the proposed design method. Sensitivity analysis is given in Section IV. Experimental verification is placed in Sections V. Finally, Section VI concludes this article.

II. Analysis of Traditional 6.78 MHz WPT System Design Method

A. Traditional 2.4 A Constant Current Output System Design

Fig. 1(a) is the traditional 6.78 MHz WPT constant current output system. It usually consists of four parts, followed by Class-E power amplifier (PA), impedance compression network, coupling coil, and Class-E rectifier. Here, $Z_{\rm pa}$ is the total load impedance that the PA drives, $Z_{\rm coil}$ is the reflection impedance of the primary side (Total system impedance as seen to the right of the T-type compression network), and $Z_{\rm rec}$ corresponds to the input impedance of the rectifier.

Simulation was performed using advanced design system software. With the help of load-pull model analysis, the characteristic curves of PA under different load impedances are obtained. As shown in Fig. 1(d), the red curve is the PA efficiency contour, and the purple curve is the PA output power contour. The specific simulation parameters of the constant current output system are also given. The ideal load impedance curve of the PA that satisfies the constant current output index can be obtained through simulation [see Fig. 1(d) blue curve]. Here, the high-efficiency operation of the constant-current PA needs to meet three requirements as follows.

1) *Sufficient power output:* The PA output impedance $Z_{\rm pa}$ corresponding to the maximum power load point should coincide with the preset PA maximum power output curve [see Fig. 1(d) yellow power contour line].
2) *Impedance compression direction:* For a constant current output system, the impedance compression direction should keep the output current constant. That is, the output power $P_{\rm H}$ is proportional to the load $R_{\rm H}$

$$\text{CCM}: P_{\rm H} \propto R_{\rm H}. \tag{1}$$

3) *Target high-efficiency area:* The PA output impedance point $Z_{\rm pa}$ generated within the load variation range falls into the target high-efficiency area as much as possible [see Fig. 1(d) yellow target area].

For high-frequency WPT systems, impedance analysis is usually performed sequentially from the output stage to the input stage. The input impedance $X_{\rm rec}$ [see Fig. 1(b) or (c)] of a high frequency system rectifier tends to exhibit nonlinear capacitive characteristics, different from low frequency rectifiers. In the case of load variation range of 18.75 Ω–30 Ω, it is necessary to design the secondary series capacitor $C_{\rm SH}$, taking into account the inductance of the secondary coil and the input impedance of the rectifier to achieve full compensation at the maximum power point, thereby improving system efficiency. The −48 Ω rectifier input reactance $X_{\rm rec}$ is compensated to 0 Ω at the 30 Ω load point, as shown by the red arrow in Fig. 1(b).

Fig. 1(c) shows the whole process of impedance transformation when the traditional high-frequency WPT system realizes constant current output. In total, 18.75 Ω–30 Ω represents the load $R_{\rm H}$ change of the battery in the 45–72 V/2.4 A constant current stage, and the specific impedance transformation value is shown in Fig. 1(b). At this time, the input impedance $Z_{\rm rec}$ (red diamond) of the rectifier and the reflected impedance $Z_{\rm coil}$ (purple diamond) of the coil seriously deviate from the PA high-efficiency range [see Fig. 1(d) yellow ideal target area]. To solve this problem, the T-LCL impedance compression network is adopted to compress the reflection impedance $Z_{\rm coil}$ to the ideal PA output impedance $Z_{\rm pa}$. It is worth noting that the $Z_{\rm pa}$ direction at this time is the direction in which the output power of the PA decreases, i.e., the direction in which the load $R_{\rm H}$ decreases. Under the condition of input voltage $V_{\rm inH} = 81$ V, it can realize 2.4 A constant current output in the load range of 18.75 Ω–30 Ω. Fig. 1(b) also shows the state stress peaks of each part of the system at this time.

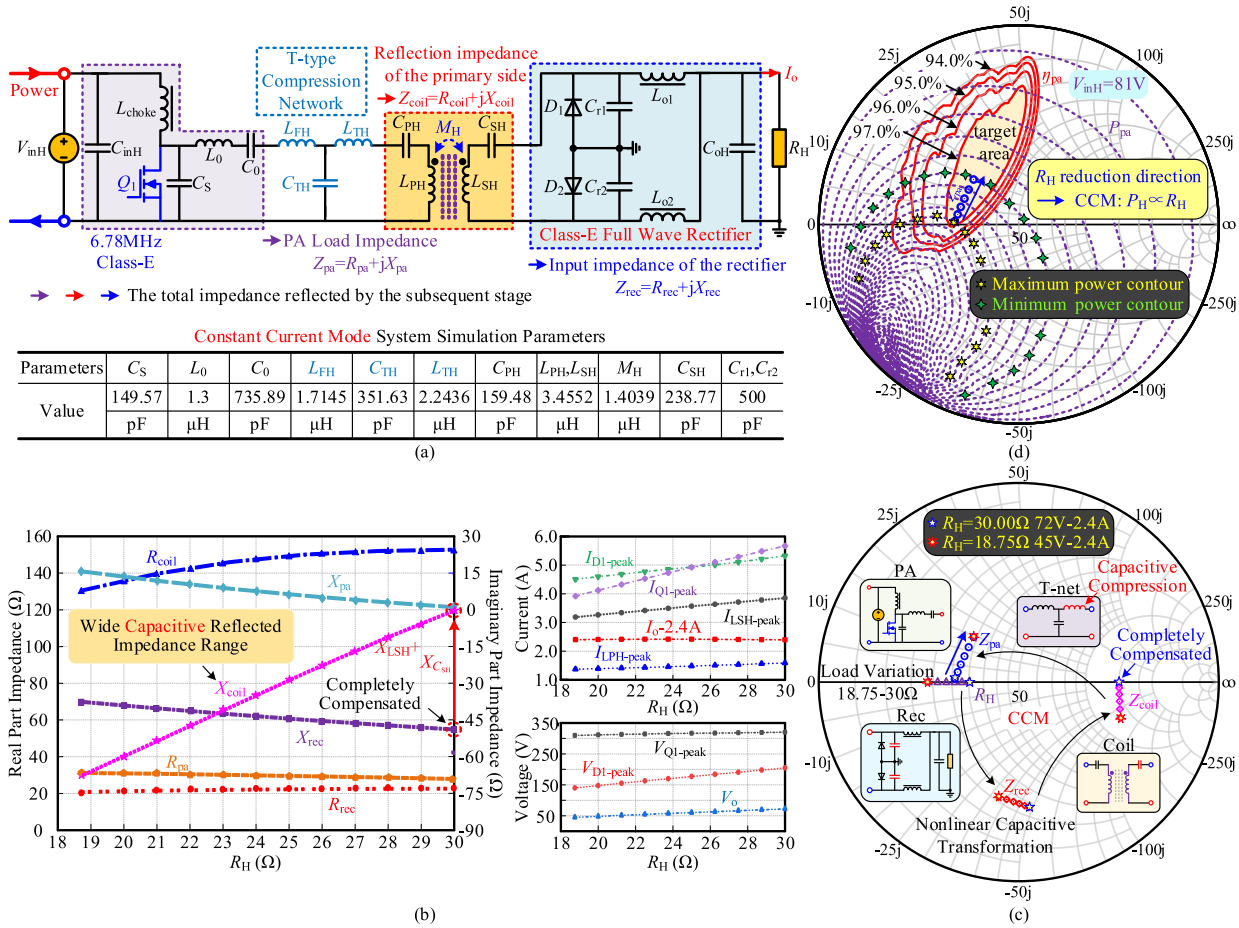

Parameters	C_S	L_0	C_0	L_{FH}	C_{TH}	L_{TH}	C_{PH}	L_{PH},L_{SH}	M_H	C_{SH}	C_{r1},C_{r2}
Value	149.57 pF	1.3 μH	735.89 pF	1.7145 μH	351.63 pF	2.2436 μH	159.48 pF	3.4552 μH	1.4039 μH	238.77 pF	500 pF

(a) (b) (c) (d)

Fig. 1. In total, 6.78 M constant current WPT system design. (a) System structure composition and specific simulation parameters. (b) Impedance transformation value and working performance of each part of the system. (c) Impedance compression process. (d) PA output performance.

B. Traditional 72 V Constant Voltage Output System Design

Fig. 2(a) is a traditional 6.78 MHz WPT constant voltage output system. Similarly, the secondary side achieves full compensation at the point of maximum power load, as indicated by the red arrow in Fig. 2(b).

In total, 30 Ω–240 Ω represents the equivalent load R_H change of the battery in the 72 V/2.4 A-0.3 A constant voltage stage. As the load R_H increases, the imaginary part X_{coil} of the coil's reflected impedance [see pink curve in Fig. 2(b)] first increases and then stabilizes, while the real part R_{coil} (blue curve) shows a trend of gradually decreasing. Correspondingly, the reflected impedance angle of the coil increases continuously, which in turn leads to an increase in reactive power and a decrease in efficiency.

In addition, compared with the constant current stage, the constant voltage stage faces a wider range of reflection impedance variation, which increases the difficulty of designing the impedance compression network. In this case, considering the change of reflection impedance in the whole range, the output impedance Z_{pa} of PA is more likely to deviate from the high-efficiency region and enter the sub-high efficiency region [see Fig. 2(d)].

Fig. 2(c) shows the whole process of impedance transformation in the constant voltage stage. At this time, the PA output power P_H is inversely proportional to the load R_H, i.e.,

$$\text{CVM}: P_H \propto \frac{1}{R_H}. \tag{2}$$

The Z_{pa} direction in Fig. 2(d) represents the direction in which the PA output power increases, i.e., the direction in which the load R_H decreases (opposite to the impedance compression direction in the constant current stage), and the system obtains the maximum power at 30 Ω. For other load points, the coil reflection impedance presents nonlinear inductive characteristics [the pink load point of Z_{coil} in Fig. 2(c)], different from the nonlinear capacitive characteristics of the constant current system at nonmaximum power load points. Therefore, a T-*LCC* type compensation network is adopted for inductive compression and capacitive compensation, replacing the T-*LCL* network in the constant voltage system.

Fig. 2(a) shows the simulation parameters of the 72 V constant voltage system, Fig. 2(b) shows the stress and impedance transformation values of each part of the system, and the input voltage is 74 V at this time. It can be seen that the stress of the PA inverter tube is about 300 V at this time, and the stress of the rectifier

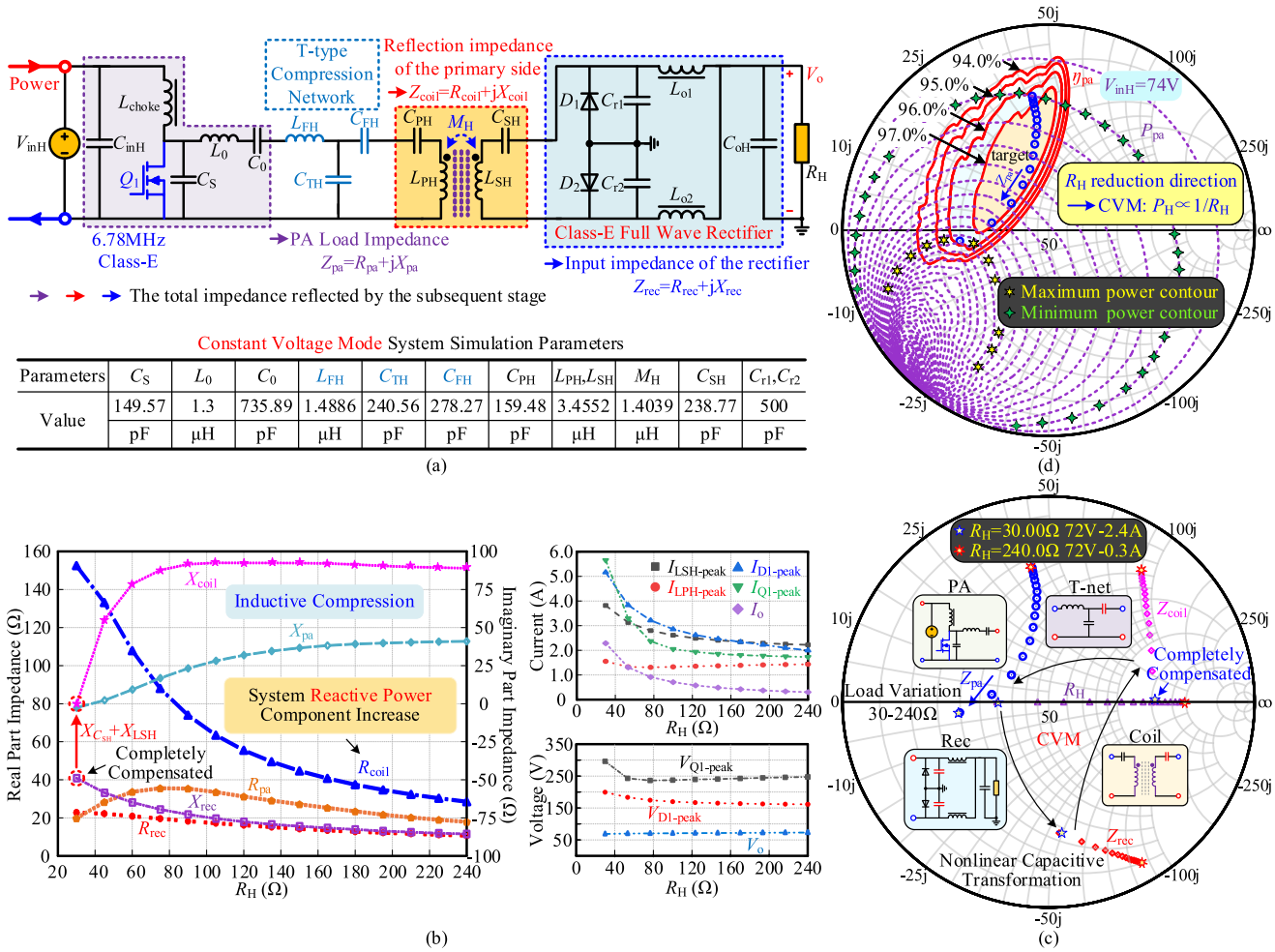

Constant Voltage Mode System Simulation Parameters

Parameters	C_S	L_0	C_0	L_{FH}	C_{TH}	C_{FH}	C_{PH}	L_{PH},L_{SH}	M_H	C_{SH}	C_{r1},C_{r2}
Value	149.57	1.3	735.89	1.4886	240.56	278.27	159.48	3.4552	1.4039	238.77	500
	pF	μH	pF	μH	pF	pF	pF	μH	μH	pF	pF

Fig. 2. In total, 6.78 M constant voltage WPT system design. (a) System structure composition and specific simulation parameters. (b) Impedance transformation value and working performance of each part of the system. (c) Impedance compression process. (d) PA output performance.

diode is also close to 200 V (the voltage tolerance of high-speed Schottky diodes is generally low), which causes difficulties in the selection of components. After all, using gallium nitride as a rectifier device requires synchronous rectification control (It is actually not easy for a 6.78 M system). Using silicon carbide means a high forward voltage drop.

So far, based on the analysis of the characteristics of the above-mentioned two traditional systems, the difficulties in system design for simultaneous CC/CV mode switching are summarized as follows.

1) *Unidirectionality of impedance compression:* In the design of constant voltage and constant current systems, the direction of impedance compression needs to follow the corresponding relationship between power and load, and there is a problem of opposite design direction.
2) *Structural differences in the impedance compression network:* Due to the different properties of the coil's reflected impedance at the nonmaximum power point, different compensation methods are required to achieve capacitive/inductive compression.
3) *Nonuniformity of input voltage:* In order to meet the high-efficiency operation and power requirements of the system, there is a problem of different input voltages in the constant voltage and constant current stage, which lacks uniformity. It will increase the difficulty of designing the bus voltage of the prestage system.
4) *High device stress:* The single-stage system completes high-voltage and high-power battery charging, and has high requirements for device stress and other aspects. In order to ensure reliable operation, it is usually necessary to sacrifice certain efficiency and maintain a sufficient level of withstand voltage margin.

III. Operating Principle and Advantages of the Proposed Wireless Battery Charging System

Fig. 3(a) shows the system structure, which also simulates the batteries charging process of 45–72 V/2.4 A and 72 V/2.4–0.3 A. The system consists of two parts: a strong robust kHz system and a high-sensitivity MHz system. The two subsystems share the same bus voltage, and the decoupling coil structure is used to avoid power crosstalk (see Fig. 4), and the output side is connected to the battery load by means of power synthesis. The kHz system completes mode switching through the poststage

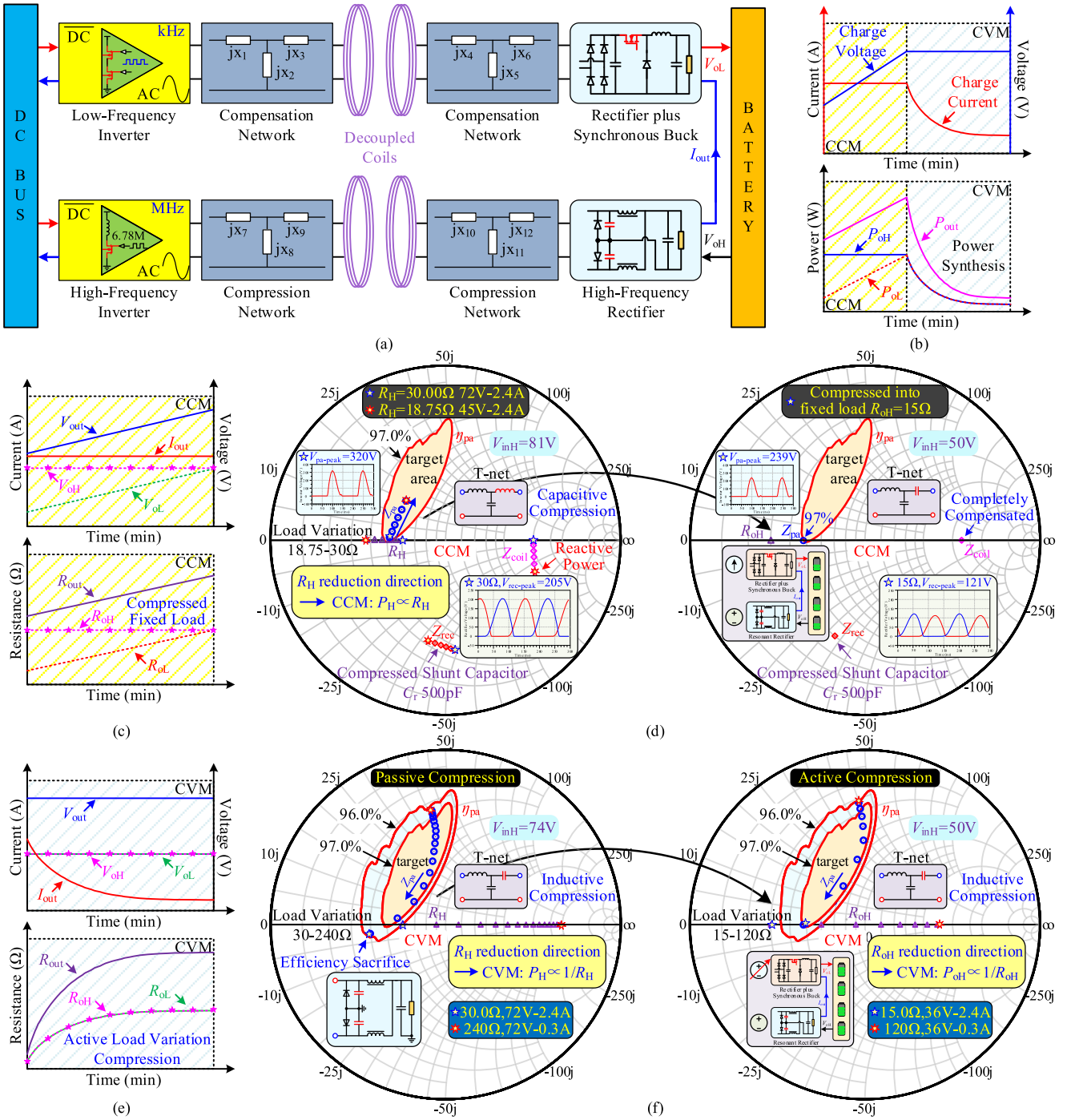

Fig. 3. Schematic of proposed charging system operation. (a) System structure. (b) Ideal charging curve. (c) Ideal output and equivalent load at CCM. (d) Comparison between the proposed system and the traditional system in CCM. (e) Ideal output and equivalent load at CVM. (f) Comparison between the proposed system and the traditional system in CVM.

dc–dc circuit, and the MHz system adopts a constant voltage design method for impedance compression and provides 36 V output. Fig. 3(b) shows the battery charging curve and the power distribution of the two subsystems under ideal conditions. P_{out}, P_{oH}, and P_{oL} represent battery charging power, high frequency (HF) output power, and low frequency (LF) output power, respectively. In CCM, the MHz system always outputs stable fixed power, and the rest of the power supplement will be completed by the kHz system. In CVM, the MHz system and kHz system will equally share all power variation. Fig. 3(c) shows the respective voltage, current and equivalent load variation of the two-channel system under ideal conditions in the CCM. V_{out} and I_{out} represent the battery charging voltage and current, respectively. V_{oH} and R_{oH} represent the output voltage and equivalent load of the HF system, respectively. V_{oL} and R_{oL} correspond to the LF system. At this time, the kHz system works

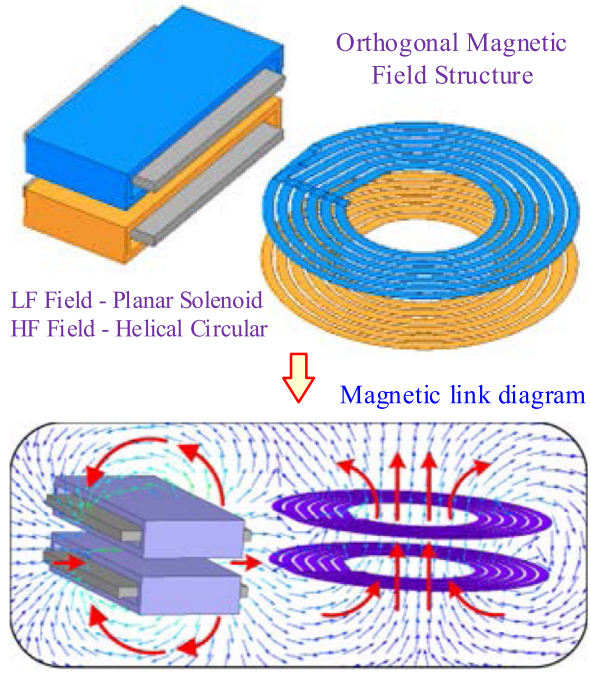

Fig. 4. Schematic diagram of decoupling coil flux linkage.

in the current source state, and the MHz system works in the constant voltage source state, so the high-frequency equivalent load R_{oH} is compressed into a fixed load point. After entering CVM [see Fig. 3(e)], the kHz system switches to the voltage source state to share the wide range of load variation faced by the MHz system.

Fig. 3(d) and (f) shows the design comparison between the traditional HF system and the proposed system under CCM and CVM, respectively. Specifically, the advantages of the proposed design method are as follows.

1) *Realize the unity of impedance compression direction:* During the whole process of battery charging, the HF system only needs to consider the constant voltage output design. R_{oH} is compressed to a fixed 15 Ω in CCM, and forms a smooth connection with the load change in CVM. The problem of impedance compression unidirectionality caused by mode switching is eliminated.
2) *Realize the unity of impedance compression network:* In the proposed design method, the reflected impedance of the HF system coil is always inductive, the compensation direction in the compression network is unified, and there is no T-*LCL*/T-*LCC* structure switching problem.
3) *Realize the unity of the input voltage:* The system input voltage is always maintained at 50 V, and there is no need to follow the adjustment according to the battery status.
4) *Realize the reduction of system stress:* The power combination technology effectively solves the problem of high voltage stress of Class-E converters. Under the same 72 V/2.4 A output condition, the stress of the switch tube is reduced from 320 V to 239 V, and the stress of the rectifier tube is reduced from 205 V to 121 V, which facilitates the selection of components and the practical application of the structure.
5) *Realize the improvement of system efficiency:* In CCM, the HF system always works in a complete resonance state, without facing the reactive components of other load points in the traditional design method. In CVM, due to the active load compression of the LF system, the actual load variation faced by the HF system is reduced by half, which greatly reduces the difficulty of impedance compression. At this time, the output impedance Z_{pa} of the PA is easier to stabilize in the target high-efficiency region, without sacrificing the efficiency of the maximum power point, and improving the system efficiency in the most critical part.

It is worth noting that, here, the kHz system is just one of the representatives of the robustness system, but not the only one. Moving a kHz system up to 1 MHz or 1.5 MHz, all operating criteria and corresponding advantages remain unchanged for the architecture shown in Fig. 3. The concept of low frequency and high frequency is only relative. In this article, 500 k is chosen as the LF system frequency for principle verification.

IV. System Sensitivity Analysis and Comparison

As mentioned in Section II, the direction of impedance compression determines the output constant capability of the HF system over the load range. In a theoretically ideal situation, the impedance compression direction is perpendicular to the PA output power contour, the distribution of load points is relatively uniform, and the output is constant. However, in the simulation, the conversion capability of the impedance compression network is limited, and it can only ensure that the PA output impedance Z_{pa} (blue circular load line) is close to the theoretical ideal curve (red arrow curve), as shown in Fig. 5. Figs. 5(a) and 6(a) correspond to the constant current system in Section II. Figs. 5(b) and 6(b) correspond to the constant voltage system in Section II. In fact, the system output voltage, current, and equivalent load variation in Sections II and III are all theoretical ideal results. Fig. 6(a) and (b), respectively, gives the output current and voltage (black square curve) of the corresponding system under simulated ideal conditions. It can be seen that in CCM, the current is relatively stable at 2.4 A and the fluctuation is small, which also corresponds to the Z_{pa} curve [see Fig. 5(a)] close to the theoretical ideal curve. However, in CVM, Z_{pa} deviates from the theoretical ideal curve. As a result, the output voltage shows a slow upward trend within the load range of this stage, and deviates from 72 V to 76.8 V at 240 Ω.

In addition, there are human factors and industrial manufacturing errors in the actual system operation, which further cause differences from the simulation ideal. Considering that there may be component parameter deviations and coil misalignment in the actual circuit, the following six simulations were carried out (see Fig. 6): all inductance parameters in the system increased or decreased by 5%; all capacitance parameters increased or decreased by 5%; mutual inductance increased or decreased 20%. It can be found that the current and voltage will seriously deviate from the charging index of the battery at 72 V/2.4 A. For the system, the following hazards will occur.

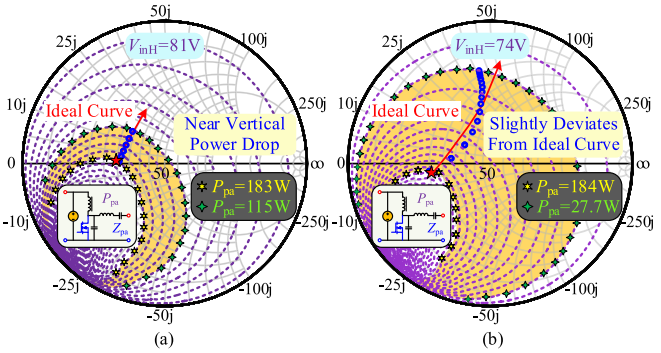

Fig. 5. Comparison of theoretical ideal and simulation ideal. (a) Constant current output system. (b) Constant voltage output system.

1) When the output current is lower than the charging current 2.4 A, and the charging speed will be reduced.
2) Severe current fluctuations will affect battery life.
3) When the output voltage is lower than the charging voltage of 72 V, the charging is too slow or even impossible to charge.
4) When the output voltage is too high and exceeds the battery voltage threshold, it brings destructive risks such as explosion.

So far, it can be found that the traditional HF system is greatly affected by parameter fluctuations, i.e., it has high sensitivity. Moreover, it is difficult to achieve accurate and constant voltage output even in the simulated ideal situation, and the reliability of the system is relatively low.

Fig. 7 shows a simplified diagram of the constant current and constant voltage stages of the proposed system. Facing the same ideal simulation state or actual parameter changes, the output fluctuations of the HF subsystem still exist (see Fig. 8).

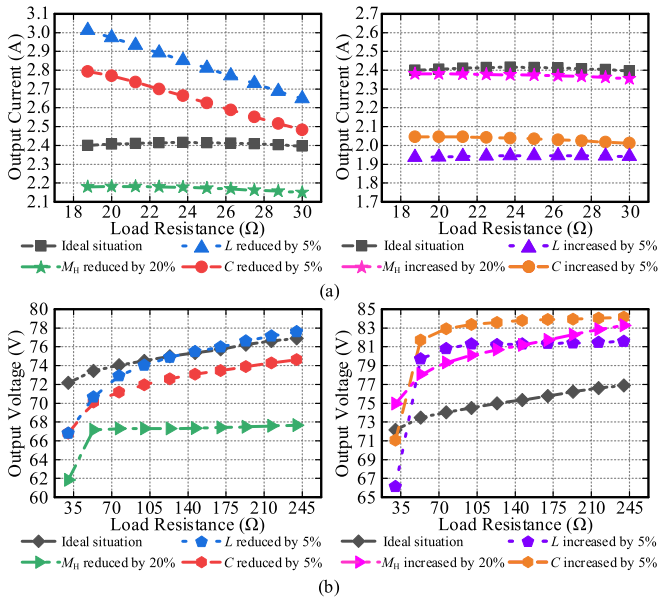

Fig. 6. Comparison of simulated ideals with actual possible situations. (a) Constant current output system. (b) Constant voltage output system.

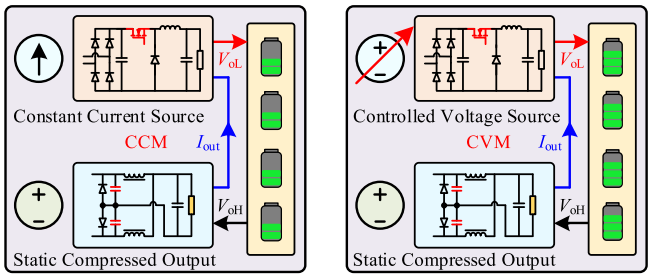

Fig. 7. Simplified diagram of the CCM and CVM of the proposed system.

$$C_{\mathrm{r}}=\frac{1}{\omega_{\mathrm{H}}R_{\mathrm{oH}}}\left[\frac{1}{4\pi}-\frac{\pi}{2}(1-D_{\mathrm{rec}})^{2}+\frac{2\pi(1-D_{\mathrm{rec}})\cos\left(\phi_{\mathrm{rec}}+2\pi D_{\mathrm{rec}}\right)-\sin\phi_{\mathrm{rec}}}{4\pi\sin\left(\phi_{\mathrm{rec}}+2\pi D_{\mathrm{rec}}\right)}\right],$$

$$\tan\phi_{\mathrm{rec}}=-\frac{\pi(1-D_{\mathrm{rec}})\sin(2\pi D_{\mathrm{rec}})+\sin^{2}(\pi D_{\mathrm{rec}})}{\pi(1-D_{\mathrm{rec}})\cos(2\pi D_{\mathrm{rec}})+\sin(\pi D_{\mathrm{rec}})\cos(\pi D_{\mathrm{rec}})} \tag{3}$$

$$R_{\mathrm{rec}}=\frac{2\sin\left(\phi_{\mathrm{rec}}+2\pi D_{\mathrm{rec}}\right)}{\pi\omega_{\mathrm{H}}C_{\mathrm{r}}}\left[\sin\left(\phi_{\mathrm{rec}}+2\pi D_{\mathrm{rec}}\right)-\sin\phi_{\mathrm{rec}}+2\pi(1-D_{\mathrm{rec}})\cos\phi_{\mathrm{rec}}+\frac{\cos\phi_{\mathrm{rec}}-\cos\left(\phi_{\mathrm{rec}}+2\pi D_{\mathrm{rec}}\right)}{4\sin\left(\phi_{\mathrm{rec}}+2\pi D_{\mathrm{rec}}\right)}\right.$$
$$\left.+\frac{\cos 2\left(\phi_{\mathrm{rec}}+2\pi D_{\mathrm{rec}}\right)-\cos 2\phi_{\mathrm{rec}}}{\tan\left(\phi_{\mathrm{rec}}+2\pi D_{\mathrm{rec}}\right)}\right] \tag{4}$$

$$X_{\mathrm{rec}}=-\frac{2\sin\left(\phi_{\mathrm{rec}}+2\pi D_{\mathrm{rec}}\right)}{\pi\omega_{\mathrm{H}}C_{\mathrm{r}}}\left[\cos\phi_{\mathrm{rec}}+2\pi(1-D_{\mathrm{rec}})\sin\phi_{\mathrm{rec}}-\frac{\sin\phi_{\mathrm{rec}}}{\tan\left(\phi_{\mathrm{rec}}+2\pi D_{\mathrm{rec}}\right)}\right.$$
$$\left.-\frac{\cos\left(\phi_{\mathrm{rec}}+2\pi D_{\mathrm{rec}}\right)}{2}+\frac{2\pi(1-D_{\mathrm{rec}})+\sin\phi_{\mathrm{rec}}\cos\phi_{\mathrm{rec}}}{2\sin\left(\phi_{\mathrm{rec}}+2\pi D_{\mathrm{rec}}\right)}\right] \tag{5}$$

$$\eta_{\mathrm{coil\_H}}=\frac{\omega_{\mathrm{H}}^{2}M_{\mathrm{H}}^{2}\left(R_{\mathrm{rec}}+r_{\mathrm{LSH}}\right)}{\omega_{\mathrm{H}}^{2}M_{\mathrm{H}}^{2}\left(R_{\mathrm{rec}}+r_{\mathrm{LSH}}\right)+r_{\mathrm{LPH}}\left(R_{\mathrm{rec}}+r_{\mathrm{LSH}}\right)^{2}+r_{\mathrm{LPH}}\left(R_{\mathrm{rec}}\tan\varphi_{\mathrm{rec-s}}\right)^{2}}\frac{R_{\mathrm{rec}}}{R_{\mathrm{rec}}+r_{\mathrm{LSH}}},$$

$$\varphi_{\mathrm{rec-s}}=\arctan\frac{\omega_{\mathrm{H}}C_{\mathrm{SH}}X_{\mathrm{rec}}+\omega_{\mathrm{H}}^{2}C_{\mathrm{SH}}L_{\mathrm{SH}}-1}{\omega_{\mathrm{H}}C_{\mathrm{SH}}R_{\mathrm{rec}}} \tag{6}$$

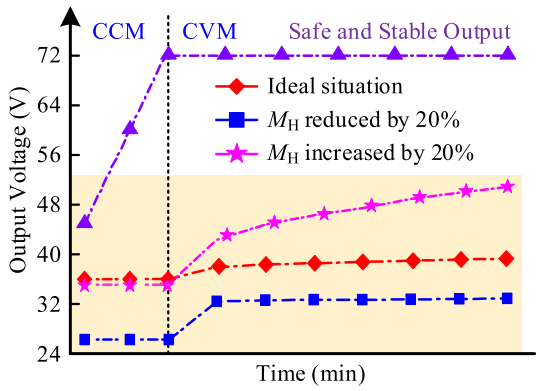

Fig. 8. Charging curve of the proposed system.

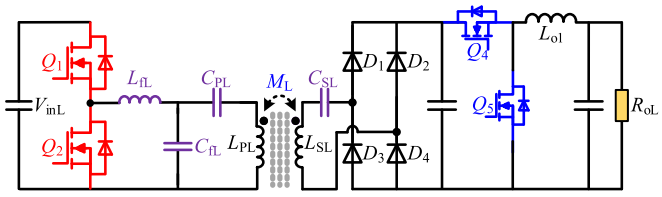

500k Subsystem Actual Parameters, V_{inL}=50V

Parameters	L_{fL}	C_{fL}	C_{PL}	L_{PL}	L_{SL}	M_L	C_{SL}	f_{Buck}
Value	1.9925	50.81	8.29	14.2	14.076	3.5865	7.19	150
	μH	nF	nF	μH	μH	μH	nF	kHz

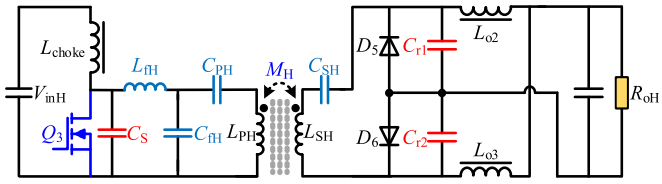

6.78M Subsystem Actual Parameters, V_{inH}=50V

Parameters	L_{fH}	C_{fH}	C_{PH}	C_S	L_{PH},L_{SH}	M_H	C_{SH}	C_{r1},C_{r2}
Value	2.0642	274.41	101.38	149.57	3.4552	1.4039	196.28	500
	μH	pF	pF	pF	μH	μH	pF	pF

Fig. 9. System experimental parameters.

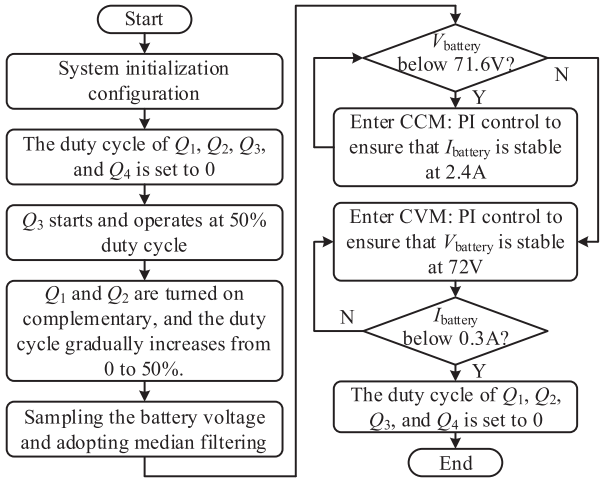

Fig. 10. System control block diagram.

However, due to the power combining mechanism, a stable and safe charging curve can still be guaranteed (Even if the LF mutual inductance fluctuates, the poststage dc–dc can still compensate), as shown in the purple curve. With the power supplement and adjustment of the LF subsystem, the operating output of the HF subsystem is given sufficient flexibility (yellow area), which solves the sensitivity problem.

V. Experimental Verification

To verify the feasibility of the proposed method, a 170 W experimental prototype was built. The parameters of each part of the system are shown in Fig. 9. For the HF subsystem, impedance compression design is the focus, which mainly includes two parts: C_r of the full-wave rectifier and T-type compression network. The value of C_r affects the rectifier input impedance change and the duty cycle D_{rec}, as shown in (3)–(5) [shown at the the bottom of previos page] [23]. For the full-wave rectifier, D_{rec} needs to be less than 0.5 to prevent shoot-through. The reduction of C_r means the increase of the rectifier input impedance real part, which can be designed to improve the coil's efficiency within a certain range [see (6), shown at the bottom of the previous page]. However, it also means the increase of the rectifier peak stress and the impedance variation range. For the maximum power point, a full compensation method is often used to improve system efficiency.

$$\mathrm{j}L_{SH}+\frac{1}{\mathrm{j}C_{SH}}+X_{rec}(P_{max})=0. \tag{7}$$

As for the impedance compression network, its parameter design mainly follows the explicit design method [24], i.e., the starting point and extension direction of the impedance trajectory are determined through three degrees of freedom in the network to adapt to the efficient operation of the PA. In this process, the adjustment of C_S is also carried out synchronously. The smaller the C_S is, the larger the efficient range of the PA is, but the output power capability decreases [25]. In short, the high-frequency parameter design process is a tradeoff process with comprehensive consideration, which needs to be adjusted repeatedly in combination with simulation. As for the LCC/S subsystem, its parameter design is relatively simple, and the traditional resonance method and fundamental wave analysis can be adopted

$$\begin{cases}\mathrm{j}X_1=\mathrm{j}\omega_L L_{fL}=\mathrm{j}\omega_L L_{PL}+\frac{1}{\mathrm{j}\omega_L C_{PL}}=-\frac{1}{\mathrm{j}\omega_L C_{fL}}\\ \mathrm{j}X_2=\mathrm{j}\omega_L L_{SL}+\frac{1}{\mathrm{j}\omega_L C_{SL}}=0.\end{cases} \tag{8}$$

The selection of switching devices and the parasitic parameters of inductors are given in Table I. Fig. 10 depicts the system control block diagram. The experimental waveform of the MHz system in the CCM is shown in Fig. 11. At this time, the state of the HF system is locked by the LF system, so the waveform of the entire constant current stage is almost unchanged. The switching voltage of the Class-E inverter drops to 0 before the drive signal arrives. The zero-voltage turn-ON of the PA switch is realized, as shown in Fig. 11(a). Although there is

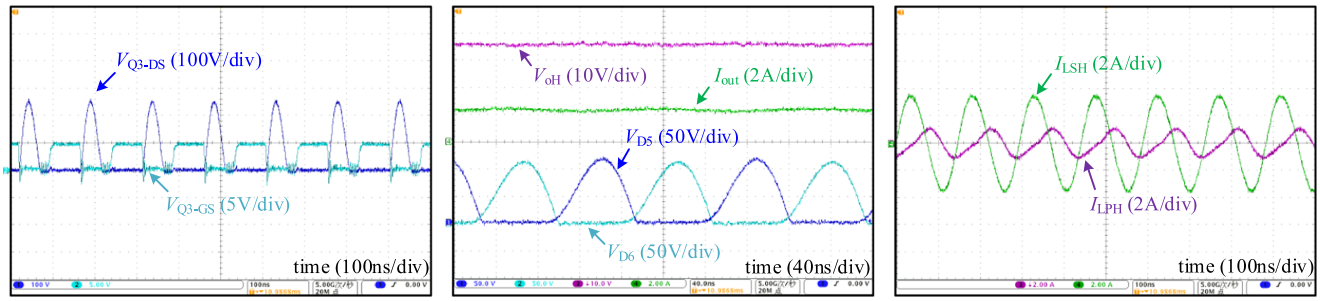

(a) (b) (c)

Fig. 11. HF subsystem at CCM. (a) PA. (b) Full wave rectification and output current. (c) Coil current.

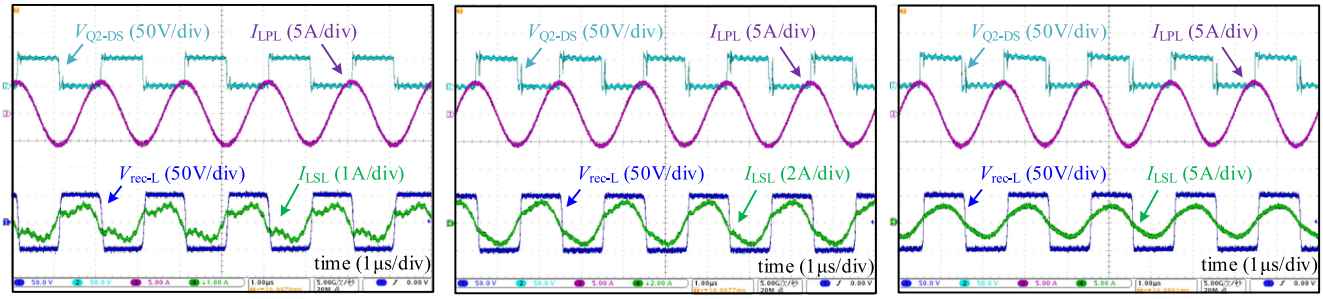

(a) (b) (c)

Fig. 12. LF subsystem inverter waveform, rectifier waveform and coil current in CCM. (a) 108 W output. (b) 140 W output. (c) 172 W output.

TABLE I
SWITCH MODEL AND INDUCTIVE ELEMENT RESISTANCE

Element	Model/Resistor
Q_1, Q_2	GS61004B
Q_3	GS-065-008-1-L
Q_4, Q_5	ISC230N10NM6
D_1-D_4	V10P10
D_5, D_6	V10P20
L_{fL}	18.965mΩ/500kHz
L_{PL}	56.234mΩ/500kHz
L_{SL}	49.843mΩ/500kHz
L_{fH}	389.62mΩ/6.78MHz
L_{PH}	753.26mΩ/6.78MHz
L_{SH}	756.34mΩ/6.78MHz
L_{choke}, L_o	15mΩ/dc

a certain reverse current conduction time, it is for compatibility with subsequent load variation during CVM. Fig. 11(b) shows the full-wave rectifier voltage, HF system output voltage, and charging current waveforms. It can be seen that although there are certain large and small waveform phenomena, they are not obvious. The HF system is stable at 36 V, and the charging current is maintained at 2.4 A, which is in line with expectations. Fig. 11(c) shows the primary and secondary current waveforms of the coil.

Figs. 12 and 13 show the changes in the working status of the LF system in CCM. Figs. 12(a) and 13(a) correspond to the output 45 V/2.4 A, Figs. 12(b) and 13(b) correspond to the output 58.5 V/2.4 A, Figs. 12(c) and 13(c) correspond to the output 72 V/2.4 A. $V_{\text{rec-L}}$ represents the full bridge rectifier input voltage.

Figs. 14, 15, and 16 describe the system state changes during CVM, corresponding to 72 V/0.3 A, 72 V/0.9 A and 72 V/2 A output conditions, respectively. Analyzing Figs. 14(a), 15(a), and 16(a), it can be observed that as the output power decreases continuously (that is, the equivalent resistance of the HF system increases), the reverse current conduction time gradually decreases. However, it has always maintained a good soft-switching characteristic and realized the high-efficiency operation of the PA in the full load range. Figs. 14(b), 15(b), and 16(b) show the variation of HF subsystem output voltage V_{oH} and battery charging voltage V_{out} with output power. It can be seen that V_{oH} is no longer a fixed 36 V, and there is a certain voltage deviation in CVM. However, V_{out} is always maintained at 72 V, which benefits from the power supplement and adjustment of the LF subsystem [see Figs. 14(c), 15(c), and 16(c)]. For Figs. 14–16(c), the $V_{\text{Q2-GS}}$ noise is caused by the dual system sharing the same voltage bus (The choke inductance L_{chock} is not large, in order to ensure better operation of the PA), but this level will not have any impact.

Fig. 17 shows the output results of each part of the proposed system during the entire simulated charging process. Fig. 17(a) shows the change curve of charging power and efficiency. In CCM, the efficiency is higher, rising from 90% to 92%. In CVM, as the equivalent load increases, the efficiency gradually decreases. Fig. 17(d) shows the change curve of charging voltage and current, which is very close to the ideal 72 V/2.4 battery charging curve. Fig. 17(b) and (c) shows the variation of power and efficiency for HF system and LF system, respectively. It can be seen that in CCM, the HF system power is compressed around 86 W. The LF system performs 22.42 W–86.44 W power supplement. In CVM, the power of HF and LF systems is not evenly distributed, and the HF system accounts for relatively more. Fig. 17(e) and (f) shows the output voltage of the two

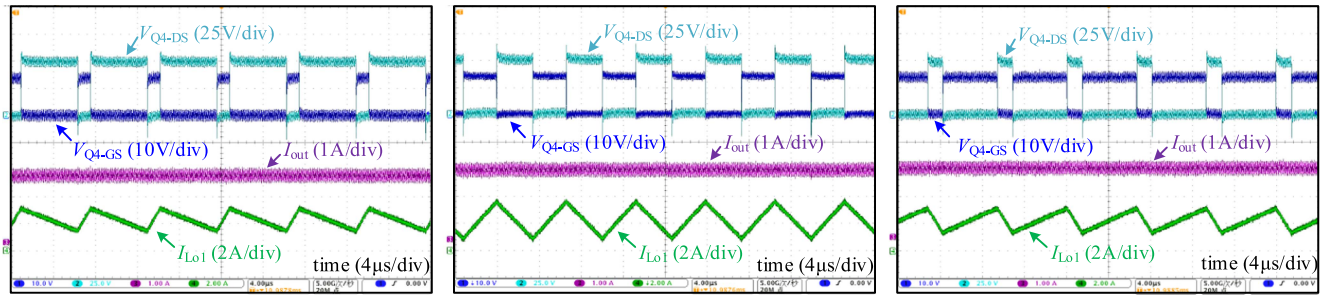

Fig. 13. LF subsystem synchronous Buck and output current waveform in CCM. (a) 108 W output. (b) 140 W output. (c) 172 W output.

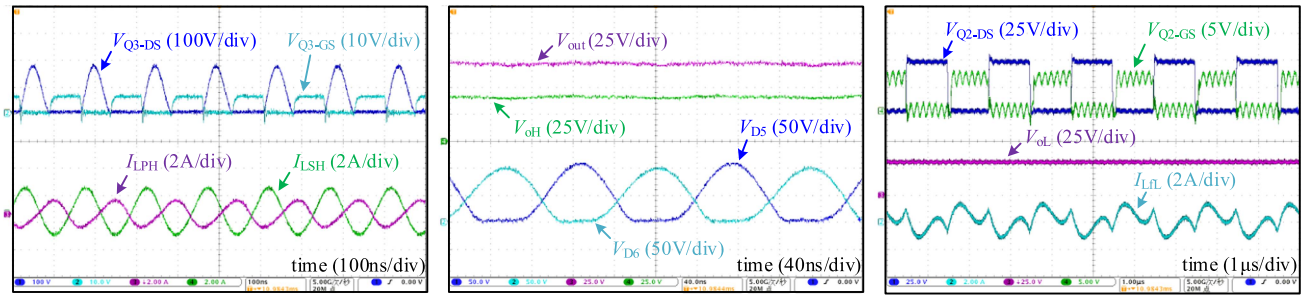

Fig. 14. In total, 21.6 W output at CVM. (a) PA and HF coil current. (b) Full wave rectification and output voltage. (c) LF subsystem.

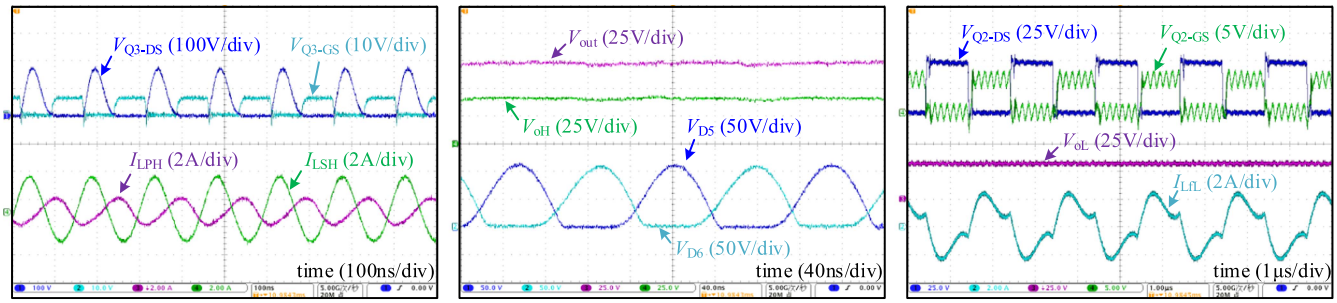

Fig. 15. In total, 64.8 W output at CVM. (a) PA and HF coil current. (b) Full wave rectification and output voltage. (c) LF subsystem.

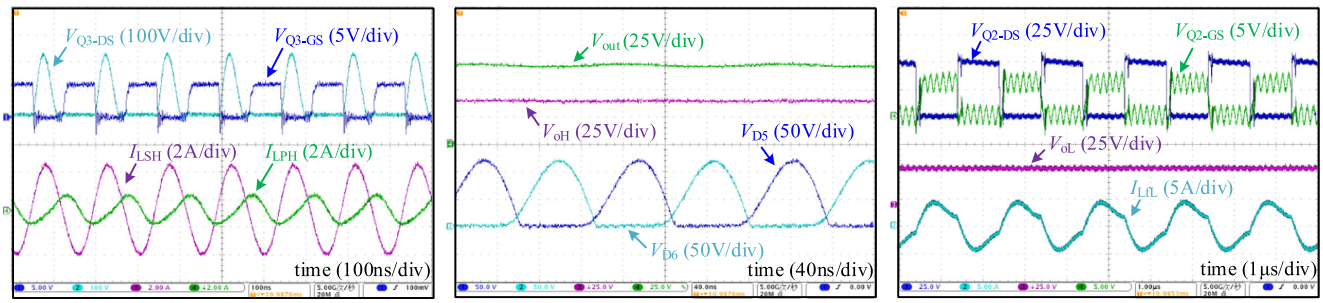

Fig. 16. In total, 144 W output at CVM. (a) PA and HF coil current. (b) Full wave rectification and output voltage. (c) LF subsystem.

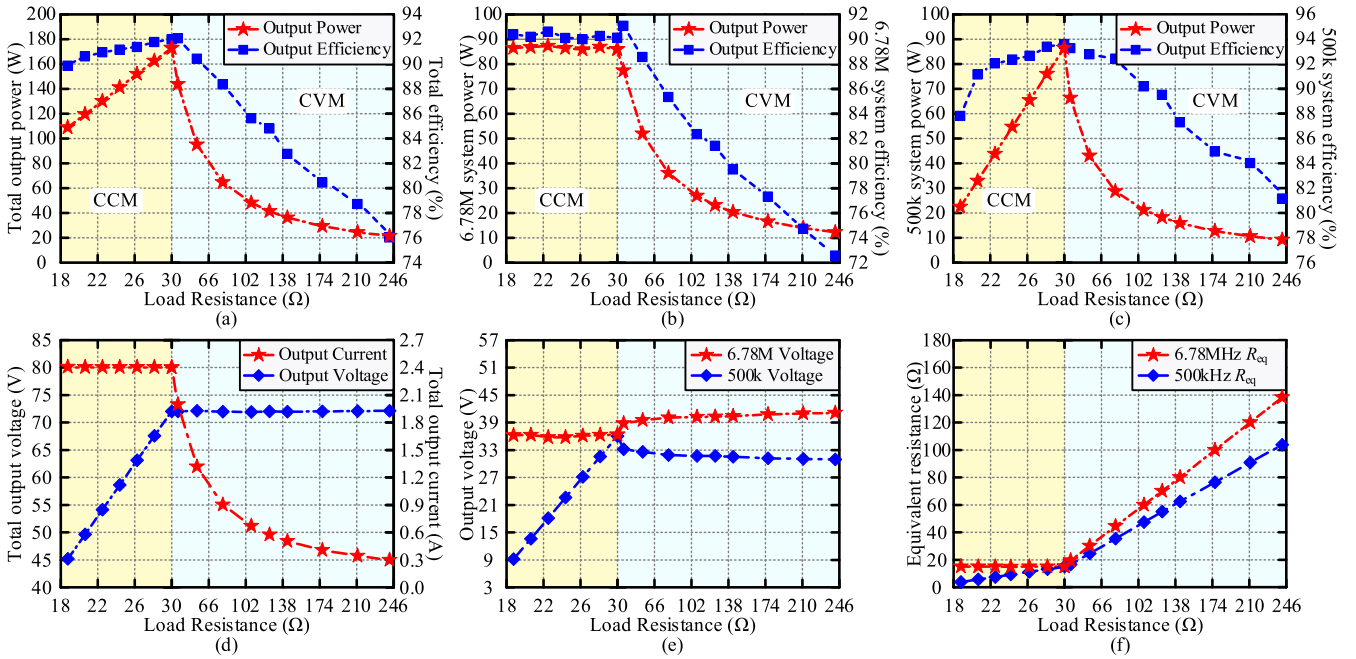

Fig. 17. Experimental results vary with battery equivalent resistance. (a) Battery charging power and efficiency. (b) HF subsystem output power and efficiency. (c) LF subsystem output power and efficiency. (d) Battery charging voltage and current. (e) HF and LF subsystems output voltage. (f) HF and LF subsystems equivalent resistance.

TABLE II
PERFORMANCE COMPARISON OF THE PROPOSED SYSTEM WITH EXISTING LITERATURES

	Power (max)	Frequency	Topology	Coupling Coefficient	CC/CV	CCM		CVM	
						Load	Efficiency	Load	Efficiency
[20]	77.4W	88.5kHz	S/S	0.21	3A/25.8V	6.7Ω-8.6Ω	74.9%-75.1%	8.6Ω-84.5Ω	75.1%-17.5%
			S/P	0.21	3A/25.8V	6.7Ω-8.6Ω	40.5%-43.5%	8.6Ω-84.5Ω	61.1%-43.5%
[12]	172.8W	500kHz	RIRC	0.49/0.7	3.6A/48V	10Ω-13.3Ω	89.5%-92.2%	13.3Ω-247Ω	92.25%-77%
[22]	120W	1MHz	AC/S	0.278	2.5A/48V	10Ω-19.2Ω	89%-91%	19.2Ω-60Ω	92.4%-89%
[21]	16.8W	6.78MHz	DCR+S/LC	0.2	1A/16.8V	14Ω-16.8Ω	78.5%-80%	16.8Ω-214Ω	85%-75.1%
[24]	40W	6.78MHz	IMN/S	0.288	CV:20-22.3V	n/a	n/a	10Ω-50Ω	84.1%-78.1%
Proposed	172.8W	6.78MHz 500kHz	T+LCC/S	0.4/0.25	2.4A/72V	18.75Ω-30Ω	90%-92.08%	30Ω-242Ω	92.08%-76%

RIRC: Reconfigurable Intermediate Resonant Circuit. AC: Active Clamp. DCR: DC Input Voltage Regulation. LC: LC-Type Impedance Compression Networks. IMN: Impedance Matching Networks. T: T-Type Impedance Compression Networks.

subsystems and the equivalent load changes, respectively. It can be seen that the output voltage of the HF system is almost stable at 36 V, and the equivalent load is compressed at 15 Ω in CCM. In CVM, as analyzed previously, the HF system still has a voltage rise phenomenon, and the resistance distribution is no longer uniform. When the battery equivalent resistance increases to 242 Ω, the HF system equivalent resistance is 138 Ω, while the LF system corresponds to 104 Ω. In order to meet the ideal effect, the LF system performs output follow compensation. The experimental system equipment is shown in Fig. 18. Table II shows the comparison between the proposed system and other existing literatures. It can be seen that the proposed system not only realizes high-frequency system CC/CV switching, but also has certain advantages in terms of power level, efficiency, and wide load range. In further research, dual-frequency integration of coupled coils and converters is expected to improve power density.

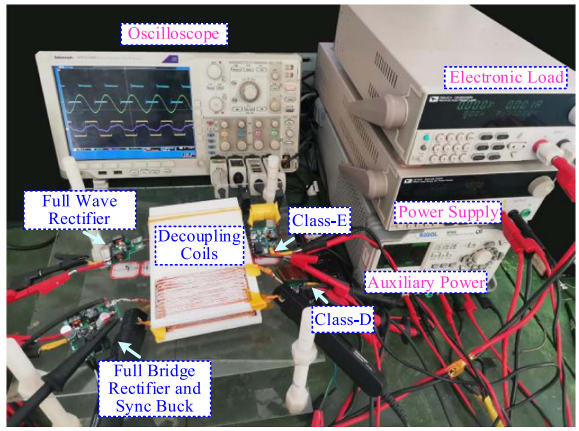

Fig. 18. Experimental prototype.

VI. Conclusion

In this article, the system characteristics of the traditional 6.78 MHz WPT constant current output and constant voltage output are analyzed in detail. The problems of inconsistent impedance compression direction, different impedance compression network structure, inconsistent bus voltage, and high system stress in the CCM and CVM are analyzed. In order to realize its high-efficiency adaptive CC/CV mode switching, a power synthesis design method is proposed. At this time, the high-frequency system only needs to consider the constant voltage design during the whole charging process, and the equivalent load in the constant current stage is locked by the low-frequency subsystem, thus solving the problem of impedance compression unidirectionality and improving system efficiency over the full load range. Furthermore, the high-sensitivity problem of the traditional high-frequency system is analyzed in detail, and the harm caused by it is also explained. While in the proposed method, the output fluctuation of the high-frequency system is given sufficient flexibility space, and the robust power compensation of the low-frequency subsystem is used to achieve accurate and stable output. Finally, the 72 V/2.4 A battery charging process is simulated through the construction of the experimental platform. In the case of 173 W output, the charging efficiency reaches 92%. The charging voltage and current curves are in line with ideal expectations.

References

[1] J. Zhao, T. Cai, S. Duan, H. Feng, C. Chen, and X. Zhang, "A general design method of primary compensation network for dynamic WPT system maintaining stable transmission power," *IEEE Trans. Power Electron.*, vol. 31, no. 12, pp. 8343–8358, Dec. 2016.

[2] M. Huang, Y. Lu, and R. P. Martins, "A reconfigurable bidirectional wireless power transceiver for battery-to-battery wireless charging," *IEEE Trans. Power Electron.*, vol. 34, no. 8, pp. 7745–7753, Aug. 2019.

[3] H. Yin, M. Fu, M. Liu, J. Song, and C. Ma, "Autonomous power control in a reconfigurable 6.78-MHz multiple-receiver wireless charging system," *IEEE Trans. Ind. Electron.*, vol. 65, no. 8, pp. 6177–6187, Aug. 2018.

[4] Y. Liu, U. K. Madawala, R. Mai, and Z. He, "Zero-phase-angle controlled bidirectional wireless EV charging systems for large coil misalignments," *IEEE Trans. Power Electron.*, vol. 35, no. 5, pp. 5343–5353, May 2020.

[5] K. Song et al., "Design of DD coil with high misalignment tolerance and low EMF emissions for wireless electric vehicle charging systems," *IEEE Trans. Power Electron.*, vol. 35, no. 9, pp. 9034–9045, Sep. 2020.

[6] A. Zakerian, S. Vaez-Zadeh, and A. Babaki, "A dynamic WPT system with high efficiency and high power factor for electric vehicles," *IEEE Trans. Power Electron.*, vol. 35, no. 7, pp. 6732–6740, Jul. 2020.

[7] C. Xiao, D. Cheng, and K. Wei, "An LCC-C compensated wireless charging system for implantable cardiac pacemakers: Theory, experiment, and safety evaluation," *IEEE Trans. Power Electron.*, vol. 33, no. 6, pp. 4894–4905, Jun. 2018.

[8] R. Guida, E. Demirors, N. Dave, and T. Melodia, "Underwater ultrasonic wireless power transfer: A battery-less platform for the Internet of Underwater things," *IEEE Trans. Mobile Comput.*, vol. 21, no. 5, pp. 1861–1873, May 2022.

[9] S. Li, Z. Liu, H. Zhao, L. Zhu, C. Shuai, and Z. Chen, "Wireless power transfer by electric field resonance and its application in dynamic charging," *IEEE Trans. Ind. Electron.*, vol. 63, no. 10, pp. 6602–6612, Oct. 2016.

[10] Z. Sun, J. Sun, Y. Wang, and D. Xu, "An efficiency optimization method based on double side impedance angle design for wireless power transfer system," *IEEE Trans. Power Electron.*, vol. 38, no. 4, pp. 5000–5012, Apr. 2023, doi: 10.1109/TPEL.2022.3232415.

[11] J. Liu, C. S. Wong, C. Sun, F. Xu, X. Jiang, and K. H. Loo, "Software-reconfigurable multi-stage constant current wireless battery charging based on multi-harmonic power transmission," *IEEE Trans. Power Electron.*, vol. 38, no. 4, pp. 5586–5597, Apr. 2023, doi: 10.1109/TPEL.2022.3232704.

[12] Y. Li et al., "Reconfigurable intermediate resonant circuit based WPT system with load-independent constant output current and voltage for charging battery," *IEEE Trans. Power Electron.*, vol. 34, no. 3, pp. 1988–1992, Mar. 2019.

[13] D. H. Tran, V. B. Vu, and W. Choi, "Design of a high-efficiency wireless power transfer system with intermediate coils for the on-board chargers of electric vehicles," *IEEE Trans. Power Electron.*, vol. 33, no. 1, pp. 175–187, Jan. 2018.

[14] Y. Zhang, Z. Shen, W. Pan, H. Wang, Y. Wu, and X. Mao, "Constant current and constant voltage charging of wireless power transfer system based on three-coil structure," *IEEE Trans. Ind. Electron.*, vol. 70, no. 1, pp. 1066–1070, Jan. 2023.

[15] X. Mao, J. Chen, Y. Zhang, and J. Dong, "A simple and reconfigurable wireless power transfer system with constant voltage and constant current charging," *IEEE Trans. Power Electron.*, vol. 37, no. 5, pp. 4921–4925, May 2022.

[16] R. Mai, Y. Chen, Y. Zhang, N. Yang, G. Cao, and Z. He, "Optimization of the passive components for an S-LCC topology-based WPT system for charging massive electric bicycles," *IEEE Trans. Ind. Electron.*, vol. 65, no. 7, pp. 5497–5508, Jul. 2018.

[17] Y. Jiang, L. Wang, Y. Wang, J. Liu, M. Wu, and G. Ning, "Analysis, design, and implementation of WPT system for EV's battery charging based on optimal operation frequency range," *IEEE Trans. Power Electron.*, vol. 34, no. 7, pp. 6890–6905, Jul. 2019.

[18] L. Wu, B. Zhang, and Y. Jiang, "Position-independent constant current or constant voltage wireless electric vehicles charging system without dual-side communication and DC–DC converter," *IEEE Trans. Ind. Electron.*, vol. 69, no. 8, pp. 7930–7939, Aug. 2022.

[19] Z. Liu, L. Wang, Y. Guo, and S. Li, "Primary-side linear control for constant current/voltage charging of the wireless power transfer system based on the LCC-N compensation topology," *IEEE Trans. Ind. Electron.*, vol. 69, no. 9, pp. 8895–8904, Sep. 2022.

[20] K. Song, Z. Li, J. Jiang, and C. Zhu, "Constant current/voltage charging operation for series-series and series–parallel compensated wireless power transfer systems employing primary-side controller," *IEEE Trans. Power Electron.*, vol. 33, no. 9, pp. 8065–8080, Sep. 2018.

[21] M. Liu, C. Zhao, J. Song, and C. Ma, "Battery charging profile-based parameter design of a 6.78-MHz class E^2 wireless charging system," *IEEE Trans. Ind. Electron.*, vol. 64, no. 8, pp. 6169–6178, Aug. 2017.

[22] H. Li, M. Liu, Y. Yang, Z. Song, and Y. Wang, "A multi-MHz active clamp topology for high cost-performance wireless power transfer," *IEEE Trans. Power Electron.*, vol. 37, no. 10, pp. 12828–12840, Oct. 2022.

[23] M. Liu, M. Fu, and C. Ma, "Low-harmonic-contents and high-efficiency class E full-wave current-driven rectifier for megahertz wireless power transfer systems," *IEEE Trans. Power Electron.*, vol. 32, no. 2, pp. 1198–1209, Feb. 2017.

[24] Y. Shao, H. Zhang, M. Liu, and C. Ma, "Explicit design of impedance matching networks for robust MHz WPT systems with different features," *IEEE Trans. Power Electron.*, vol. 37, no. 9, pp. 11382–11393, Sep. 2022.

[25] Y. Wang, Z. Sun, Y. Guan, and D. Xu, "Overview of megahertz wireless power transfer," *Proc. IEEE*, vol. 111, no. 5, pp. 528–554, May 2023.

Zhan Sun (Student Member, IEEE) was born in Heilongjiang Province, China, in 1997. He received the B.S. and M.S. degrees in 2019 and 2021, respectively, from Harbin Institute of Technology, Harbin, China, where he is currently working toward the Ph.D. degree all in electrical engineering.

His research interests include wireless power transfer, magnetic coupling structure design, high frequency, and very high frequency converters.

Yingchao Chi (Graduate Student Member, IEEE) was born in Shandong Province, China, in 2000. She received the B.S. degree from Yanshan University, Qinhuangdao, China, in 2018. She is currently working toward the M.S. degree from Harbin Institute of Technology, Harbin, China, all in electrical engineering.

Her current research interests include wireless power transfer and high-frequency high-density power converters.

Yijie Wang (Senior Member, IEEE) was born in Heilongjiang Province, China, in 1982. He received the B.S., M.S., and Ph.D. degrees in electrical engineering from Harbin Institute of Technology, Harbin, China, in 2005, 2007, and 2012, respectively.

From 2012 to 2014, he was a Lecturer with the Department of Electrical and Electronics Engineering, Harbin Institute of Technology. From 2014 to 2017, he was an Associate Professor with the Department of Electrical and Electronics Engineering, Harbin Institute of Technology. Since 2017, he has been a Professor with the Department of Electrical and Electronics Engineering, Harbin Institute of Technology. His research interests include dc–dc converters, soft-switching power converters, power factor correction circuits, digital control electronic ballasts, and LED lighting systems.

Dr. Wang is an Associate Editor for the IEEE TRANSACTIONS ON INDUSTRIAL ELECTRONICS, IEEE JOURNAL OF EMERGING AND SELECTED TOPICS IN POWER ELECTRONICS, *IEEE Access*, *IET Power Electronics,* and *Journal of Power Electronics*.

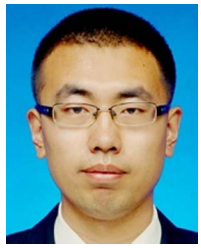

Yueshi Guan (Senior Member, IEEE) was born in Heilongjiang, China, in 1990. He received the B.S., M.S., and Ph.D. degrees in electrical engineering from the Harbin Institute of Technology (HIT), Harbin, China, in 2013, 2015, and 2019, respectively.

Since 2019, he has been an Associate Professor with the Department of Electrical and Electronics Engineering, HIT. His research interests include the areas of high-frequency and very high-frequency converters, single-stage ac/dc converter, and light-emitting diode lighting systems.

Dianguo Xu (Fellow, IEEE) received the B.S. degree in control engineering from Harbin Engineering University, Harbin, China, in 1982, and the M.S. and Ph.D. degrees in electrical engineering from Harbin Institute of Technology (HIT), Harbin, China, in 1984 and 1989, respectively.

In 1984, he was with the Department of Electrical Engineering, HIT as an Assistant Professor. Since 1994, he has been a Professor with the Department of Electrical Engineering, HIT. He was the Dean with the School of Electrical Engineering and Automation, HIT, from 2000 to 2010. He was the Vice President with HIT, from 2014 to 2020. He has authored and coauthored more than 600 technical papers. His research interests include renewable energy generation technology, power quality mitigation, sensorless vector controlled motor drives, and high performance servo system.

Dr. Xu is a Chairman of IEEE Harbin Section, Co-EIC of IEEE TRANSACTIONS ON POWER ELECTRONICS, Associate Editor for the IEEE TRANSACTIONS ON INDUSTRIAL ELECTRONICS, IEEE JOURNAL OF EMERGING AND SELECTED TOPICS IN POWER ELECTRONICS. He was the recipient of the 2018 IEEE IAS Outstanding Achievement Award.